Insect normal hovering flight in ground effect

Tong Gao and Xi-Yun Lu[a)]
Department of Modern Mechanics, University of Science and Technology of China, Hefei, Anhui 230026, People's Republic of China

(Received 25 December 2007; accepted 10 June 2008; published online 5 August 2008)

The ground effect on insect normal hovering is investigated using an immersed boundary-lattice Boltzmann method to solve the two-dimensional incompressible Navier–Stokes equations. A virtual model of an elliptic foil with oscillating translation and rotation near a body surface or ground is used. Computations have been carried out for some parameters including the distance between the foil and the surface, phase difference between the rotation and translation, and amplitude of oscillating rotation. The ground effect on the unsteady forces and vortical structures is analyzed. In particular, three typical regimes of force behavior due to the ground effect, i.e., force enhancement, force reduction, and force recovery regime, are identified and closely associated with the evolution of vortex structures. The results obtained in this study provide physical insight into the understanding of aerodynamics and flow structures for insect normal hovering flight with a ground effect and flying mechanisms relevant to insect perching on body. © *2008 American Institute of Physics*. [DOI: 10.1063/1.2958318]

I. INTRODUCTION

Insect flying through air has developed the superior and complete performance of flying in complex environments. In nature, flying insect usually perches on some bodies and the ground effect will play a significant influence on the flying performance.[1] The relevant aerodynamic characteristics are helpful for understanding the flight stability of biomimic man-made machines.[2,3] However, to our knowledge, the ground effect on the insect flying behaviors has never been studied and is highly desired. We will thus investigate the ground effect on the insect hovering in the present paper. Moreover, extensive work on the unsteady mechanisms in insect flight has been carried out experimentally and numerically and will be briefly reviewed below.

The flow around the insect wing has been studied experimentally to exhibit the complex behaviors with highly unsteady and vortical structures.[4–12] Experiments have verified that the leading-edge vortex (LEV) over the insect wing plays the most important aspect in insect flight to significantly generate the lift during the translation of the flapping wing.[7–12] Moreover, it is also found that the lift can be enhanced by rotational effect and wake capture.[13] Using an analysis of the momentum imparted to the fluid by the vortex wake, the LEV can explain the high lift on the insect wing. This high lift mechanism is called the delayed stall (or dynamic stall) mechanism.[9,13] In the experiment of a model of the fruit fly,[10,13] large lift and drag peaks occur at the beginning and the end of the stroke in the case of advanced rotation, i.e., wing rotation preceding the stroke reversal, in addition to the large lift and drag during the translational phase of a stroke. The force peaks at the beginning of the stroke can be explained by the wake capture mechanism. Basically, these involved mechanisms about the high lift on the insect wing have been analyzed in detail.[9–13]

The unsteady mechanisms in insect flight have also been investigated by numerical simulations.[14–21] Liu *et al.*[14,15] first carried out a numerical simulation to deal with unsteady aerodynamics around a flapping wing mimicking moth's forewing and hindwing. Then, to supplement experiments, extensive numerical studies have been performed to reveal the mechanisms relevant to insect flight performance.[16–24] Although the major work was done based on two-dimensional (2D) simulations, we should remind the role of three dimensionality on stabilizing LEV of the flapping wing and enhancing lift production. Liu *et al.*[15] have indicated that a LEV with axial flow is detected during translational motions of three-dimensional (3D) flapping wing, causing a negative pressure distribution and enhancing lift production. The axial flow is induced by the spanwise pressure gradient and can stabilize the LEV.

Given the complexity and expensive cost of modeling fluid flows in three dimensions,[18,24] it is reasonable to employ a 2D simulation to study the mechanisms in flapping flight. A much smaller spanwise flow, about 2%–5% of the tip velocity over a dynamically scaled mechanic fruit fly wing at Reynolds number around 150, was experimentally determined by Birch and Dickinson.[11] Smoke visualization of free-flying butterflies also did not observe substantial spanwise flow, but reported high variability of 3D flow patterns.[5] It is likely that the spanwise flow within the vortex core occurs only at sufficiently large Reynolds number as in the case of a hawkmoth, but not at low Reynolds number as in the case of a fruit fly. Computed forces on a 3D dragonfly wing match ones obtained in 2D computations, despite the differences in the LEV structures.[25] Recently, Wang *et al.*[20] also confirmed that the unsteady forces predicted by 2D computation agree well with 3D experimental data, in particular, in the case of advanced and symmetric rotation of

[a)]Author to whom correspondence should be addressed. Telephone: +86-551-3603223. Electronic mail: xlu@ustc.edu.cn.

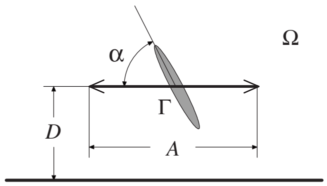

FIG. 1. Sketch of a foil in normal hovering motion of insect flight near a surface.

flapping wing. Thus, a 2D approach can be reasonably employed to predict the aerodynamic behaviors of insect flight.

In the present study, a 2D virtual model, which is an elliptic foil with oscillating translation and rotation near a surface, is used to deal with the ground effect on insect hovering motion. Although we recognize the limitation of this model, we nevertheless feel that the results will be of help in physical understanding of the relevant mechanisms for insect perching on body. To deal with the unsteady forces and flow structures, the 2D incompressible Navier–Stokes equations are solved using an immersed boundary-lattice Boltzmann method (IB-LBM), which can be convenient to treat the flapping foil boundary and the fixed ground boundary.[21,26–30]

This paper is organized as follows. The physical problem and mathematical formulation are described in Sec. II. The numerical method and validation are given in Sec. III. The ground effect on the unsteady forces and vortical structures is discussed in Sec. IV. Finally, concluding remarks are given in Sec. V.

II. PHYSICAL PROBLEM AND MATHEMATICAL FORMULATION

To investigate the flow around an elliptic foil with oscillating translation and rotation near a ground, as shown in Fig. 1, the incompressible Navier–Stokes equations are used and given as

$$\frac{\partial \mathbf{u}}{\partial t} + \mathbf{u}\cdot\nabla\mathbf{u} = -\frac{1}{\rho}\nabla p + \nu\nabla^2\mathbf{u}, \tag{1}$$

$$\nabla\cdot\mathbf{u} = 0, \tag{2}$$

where $\mathbf{u}$ is the velocity, p the pressure, ρ the density of the fluid, and ν the kinematic viscosity, respectively.

The flapping motion of insect wing in Fig. 1 can be described as[19,20]

$$A(t) = A_m\cos(2\pi t/T), \tag{3}$$

$$\alpha(t) = \alpha_0 - \alpha_m\sin(2\pi t/T + \phi), \tag{4}$$

where T is the period, A_m is the amplitude of oscillating translation, α_0 and α_m are the mean angle of attack and amplitude of oscillating rotation, respectively, and ϕ is the phase difference between the rotation and translation.

We use the chord length of the foil c and the velocity U, related to the oscillating translation $U=2\pi A_m/T$, as the length and velocity scales, respectively.[20] Then, the Reynolds number is defined as $\mathrm{Re}=\rho Uc/\nu$. The corresponding nondimensional variables shown in Eqs. (3) and (4) are still represented by the same symbols for writing convenience. To deal with the ground effect on insect flight, another parameter D is introduced to represent the distance between the foil and the ground, or called the ground clearance.[31,32] In the present calculation, no-slip boundary condition is used on the foil and ground surface, and the boundary normal derivatives of velocity vanish on the top boundary and the two vertical boundaries.

The total force acting on the flapping foil consists of the friction and pressure. Since a normal hovering is considered, the vertical and horizontal force coefficients are used and defined as $C_V=F_V/(0.5\rho U^2c)$ and $C_H=F_H/(0.5\rho U^2c)$, respectively, where F_V and F_H are the vertical and horizontal forces calculated by integrating the viscous stress and pressure along the foil.

III. NUMERICAL METHOD AND VALIDATION

To solve Eqs. (1) and (2), an IB-LBM (Refs. 27–30) is used. In the immersed boundary method,[33,34] two sets of coordinates are employed. As shown in Fig. 1, the fluid domain Ω is represented by the Eulerian coordinates $\mathbf{x}$ and the foil boundary Γ is denoted by the Lagrangian coordinates $\mathbf{X}(s,t)$ with M Lagrangian boundary points uniformly distributed. An external force $\mathbf{f}(\mathbf{x},t)$ is directly introduced in the right-hand side of Eq. (1) to mimic the boundary immersed in the fluid flow. Based on the *Proteus* method proposed by Feng and Michaelides,[30] $\mathbf{f}(\mathbf{x},t)$ can be obtained by

$$\begin{aligned}\mathbf{f}(\mathbf{x},t) &= \int_\Gamma \mathbf{F}(s,t)\delta[\mathbf{x}-\mathbf{X}(s,t)]ds \\ &= \sum_{m=1}^{M}\hat{\mathbf{f}}[\mathbf{X}(s,t)]D_s[\mathbf{x}-\mathbf{X}_m(s,t)]h\delta_s,\end{aligned} \tag{5}$$

where $\mathbf{F}(s,t)$ is the surface force density, $\hat{\mathbf{f}}[\mathbf{X}(s,t)]$ is the flow force density at the Lagrangian points, and h is the uniform lattice spacing. δ_s is the arch length between two intersections of the boundary Γ. D_s is a smoothed approximation of the 2D Dirac δ function,[34]

$$D_s(\mathbf{x}-\mathbf{X}_m) = \frac{1}{h^2}\delta_h\left(\frac{x-X_m}{h}\right)\delta_h\left(\frac{y-Y_m}{h}\right)$$

and

$$\delta_h(r) = \begin{cases}\dfrac{1}{4}\left[1+\cos\left(\dfrac{\pi r}{2}\right)\right], & |r|\leqslant 2\\ 0, & |r|>2.\end{cases}$$

Moreover, the time-discretized Lagrangian force density $\hat{\mathbf{f}}[\mathbf{X}(s,t)]$ can be constructed by the direct forcing method,[26,30]

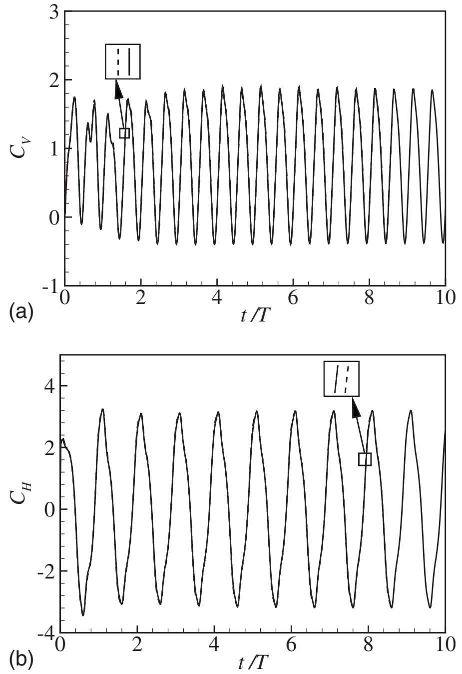

FIG. 2. Time-dependent vertical (a) and horizontal (b) force coefficients of normal hovering motion near the ground for $D=1$, $\alpha_m=45°$, and $\phi=0°$. Solid lines: $\Delta x=0.025$ with the computational domain $[-10,10]$ in the x-direction and [0, 12] in the y-direction; dashed lines: $\Delta x=0.0125$ with $[-20,20]$ in the x-direction and [0, 24] in the y-direction.

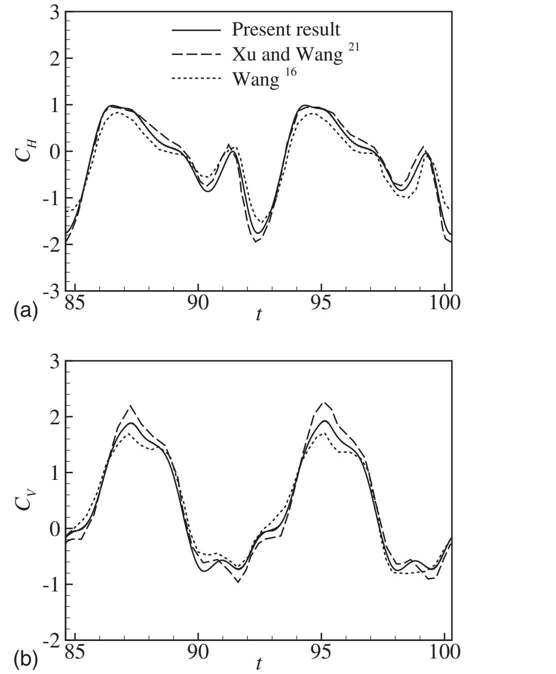

FIG. 3. Comparison of the present result and previous data for the horizontal (a) and vertical (b) force coefficients during two strokes for dragonfly hovering flight with the stroke plane inclined at an angle of $\pi/3$, Re=157, $\alpha_m=45°$, $\phi=0°$, and $A_m=1.25$.

$$\hat{f}_i^{n+1} = \rho \left.\left(\frac{U_i^{n+1} - U_i^n}{\Delta t}\right)\right|_\Gamma + RHS^n, \tag{6}$$

where U_i is the prescribed velocity of the moving boundary Γ and RHS^n includes the convective, pressure, and viscous terms at the nth time level. The Eulerian force density $\mathbf{f}(\mathbf{x},t)$ is then solved by substituting $\hat{\mathbf{f}}[\mathbf{X}(s,t)]$ into Eq. (5).

The LBM is an approach to solve fluid dynamics problem based on microscopic kinetic models.[35] To calculate Eqs. (1) and (2), an additional term is included in the discrete lattice Boltzmann equation and given as[36]

$$f_i(\mathbf{x}+\mathbf{e}_i\Delta t, t+\Delta t) - f_i(\mathbf{x},t) = -\frac{1}{\tau}[f_i(\mathbf{x},t) - f_i^{\mathrm{eq}}(\mathbf{x},t)] + \Delta t F_i, \tag{7}$$

where $f_i(\mathbf{x},t)$ is the distribution function for particles with velocity $\mathbf{e}_i$ at position $\mathbf{x}$ and time t, Δt is the time increment, and τ is the relaxation time. The D2Q9 model[37] is used in the present computation, and the equilibrium distribution function f_i^{eq} is defined as

$$f_i^{\mathrm{eq}} = \omega_i \rho\left[1 + \frac{\mathbf{e}\cdot\mathbf{u}}{c_s^2} + \frac{\mathbf{uu}:(\mathbf{e}_i\mathbf{e}_i - c_s^2\mathbf{I})}{2c_s^4}\right],$$

where ω_i is the weighing factor, c_s is the sound speed, ρ and $\mathbf{u}$ are the fluid density and velocity, respectively, and can be obtained by the distribution function, accounting for the external force $\mathbf{f}(\mathbf{x},t)$,

$$\rho = \sum_i f_i, \tag{8}$$

$$\rho\mathbf{u} = \sum_i \mathbf{e}_i f_i + \frac{1}{2}\mathbf{f}\Delta t. \tag{9}$$

Additionally, the forcing term in Eq. (7) is determined by

$$F_i = \left(1 - \frac{1}{2\tau}\right)\omega_i\left[\frac{\mathbf{e}_i - \mathbf{u}}{c_s^2} + \frac{\mathbf{e}\cdot\mathbf{u}}{c_s^4}\mathbf{e}_i\right]\cdot\mathbf{f}. \tag{10}$$

The computational loop to advance the solution from one time level to the next in the IB-LBM solver consists of the following three substeps. First, we solve the flow force density at the Lagrangian points $\hat{\mathbf{f}}[\mathbf{X}(s,t)]$ from Eq. (6) and update the Eulerian force density $\mathbf{f}(\mathbf{x},t)$ from Eq. (5). Then, $\mathbf{f}(\mathbf{x},t)$ is substituted into Eq. (10) to calculate the forcing term, and the distribution function is updated by Eq. (7). The last step is that Eqs. (8) and (9) are solved for the new density ρ and velocity $\mathbf{u}$.

To validate the present code and method, some typical flows were examined.[27,28] We also performed extensive convergence checks and validations. The time-dependent vertical and horizontal coefficients for a flapping foil near a ground calculated by different lattice spacings are shown in Fig. 2. The results by different computational conditions agree well with each other. It can be confirmed that the computed results are independent of the lattice spacing and computational domain size. To keep an accurate prediction, the results given below were calculated by the finer grid and larger domain, i.e., $\Delta x=0.0125$ with a computational domain $[-20,20]$ in the x-direction and [0, 24] in the y-direction. Moreover, to perform quantitative comparison with the literature, we have calculated some no-ground cases. As a

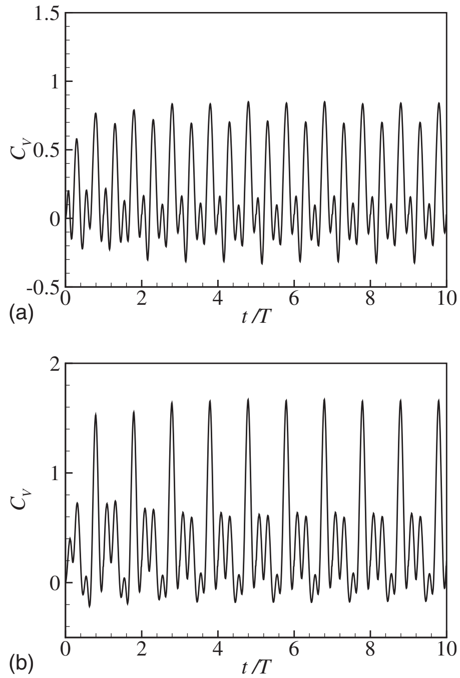

FIG. 4. Time-dependent vertical force coefficient of normal hovering motion near the ground for $D=2.5$ (a) and 5.0 (b).

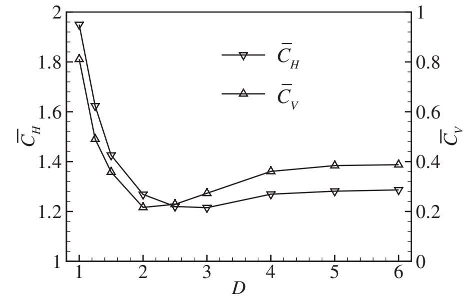

FIG. 5. Mean horizontal ($\bar{C}_H$) and vertical ($\bar{C}_V$) force coefficients vs D for $\alpha_m=45°$ and $\phi=0°$.

typical case, Fig. 3 shows the time-dependent horizontal and vertical force coefficients during two strokes for dragonfly hovering flight. This case has been carefully studied by Wang[16] and Xu and Wang.[21] It is seen that our result agrees well with the data obtained by using different numerical methods.[16,21]

IV. RESULTS AND DISCUSSION

In this section, we present some typical results on the force behaviors and vortical structures for a flapping foil near a ground. Based on the selected parameters in modeling insect hovering,[16–21] the parameters used here are given as follows: the amplitude of rotation $\alpha_m=30°$, 45°, and 60°, the mean angle of attack $\alpha_0=90°$, the amplitude of translation $A_m=1.25$, the phase difference $\phi=-45°$, 0°, and 45°. The Reynolds number Re is 100, corresponding to the flight condition of the fruit fly, and the thickness ratio of the foil is 0.25. To deal with the ground effect, the ground clearance D ranges from 1 to 6.

A. Ground effect on force behaviors

The aerodynamic forces acting on the flapping foil are directly associated with the study of insect flight. Here we first investigate the ground effect on the forces. Based on our calculations, periodic or quasiperiodic variations of time-dependent forces are achieved after three to five strokes for all the cases considered. Typically, Fig. 4 shows the time-dependent vertical force coefficient for $D=2.5$ and 5. From Figs. 2 ($D=1$) and 4 ($D=2.5$ and 5), the time-dependent forces exhibit periodic changes from the fourth stroke. The time-averaged values used below are obtained over several strokes in the periodic or quasiperiodic state. Because the horizontal force cancels almost over a period, as suggested in previous work,[20] its absolute value is used when taking the average.

The time-averaged force coefficients $\bar{C}_V$ and $\bar{C}_H$ versus the ground clearance D are shown in Fig. 5. To deal with the ground effect on the forces, the forces acting on the foil without the ground effect (or denoted by $D=\infty$) for $\alpha_m=45°$ and $\phi=0°$ are also calculated with $\bar{C}_{V\infty}=0.39$ and $\bar{C}_{H\infty}=1.28$ approximately. As D increases, the vertical force $\bar{C}_V$ decreases quickly to a minimum at $D=2$ approximately, then increases gradually and approaches to $\bar{C}_{V\infty}$. Similarly, the horizontal force $\bar{C}_H$ decreases to a minimum at $D=3$ approximately and increases to $\bar{C}_{H\infty}$.

Based on the force coefficients, we have identified three regimes of force behavior due to the ground effect, i.e., force enhancement, force reduction, and force recovery regime. From Fig. 5, as $D<1.5$, $\bar{C}_V$ and $\bar{C}_H$ are enhanced and the force behavior belongs to the force enhancement regime. As $1.5<D<3.5$, $\bar{C}_V$ and $\bar{C}_H$ are obviously less than $\bar{C}_{V\infty}$ and $\bar{C}_{H\infty}$ with the force behavior lying in the force reduction regime. As D increases further, say $D>3.5$ in Fig. 5, the ground effect becomes weak and $\bar{C}_V$ and $\bar{C}_H$ gradually increase to approaching $\bar{C}_{V\infty}$ and $\bar{C}_{H\infty}$. For neatness, we classify this force variation as a force recovery region. Further, we have examined our extensive results for different parameters shown below and identified that there exist such the three regimes of the force behavior.

To understand the underlying physical mechanisms relevant to the three force regimes, we further discuss the time-dependent force here and the vortical structures in the following subsection. For clearly exhibiting the force variation, the time-dependent force coefficients C_V and C_H over only one stroke after reaching a periodic state are shown in Fig. 6. It is seen that two peaks of C_V occur in the stroke at $D=1$. As D increases, e.g., $D=2.5$ and 5, four peaks of C_V appear in the stroke and the fourth peak value at $t/T=0.8$ approximately becomes higher. This behavior is closely associated with the time development of vortex structures near the flapping foil and will be discussed below.

At $D=1$, lying in the force enhancement region, a large C_V is generated over the forth (i.e., first half-stroke) and back (i.e., second half-stroke) strokes with two peaks at $t/T=0.15$ and 0.65 approximately. Correspondingly, C_H also

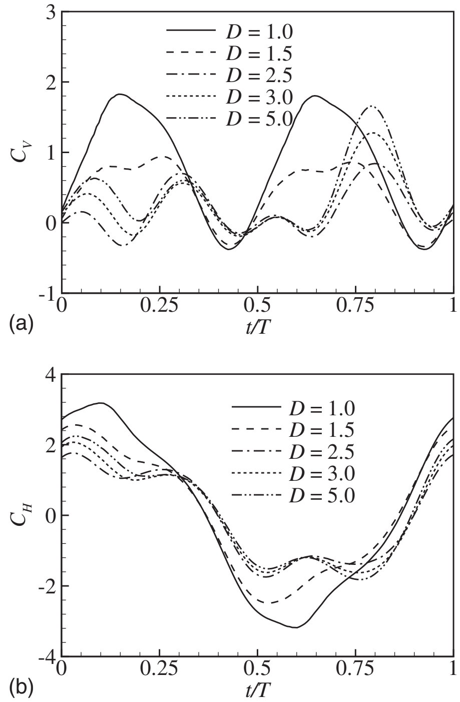

FIG. 6. Time-dependent vertical (a) and horizontal (b) force coefficients during one stroke for $\alpha_m=45°$ and $\phi=0°$.

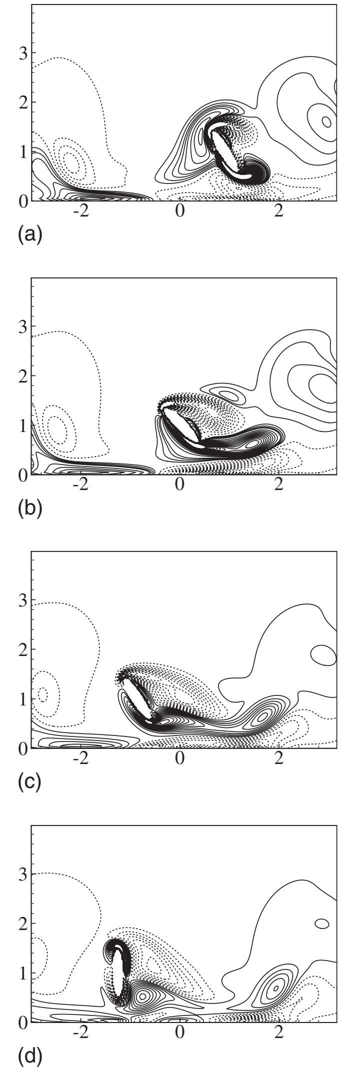

FIG. 7. Vorticity contours during the forth stroke (or the first half-stroke) for $D=1$, $\alpha_m=45°$, and $\phi=0°$ at $t/T=$(a) 1/8, (b) 2/8, (c) 3/8, and (d) 4/8. Here, solid lines represent positive values (i.e., counterclockwise vortex) and dashed lines negative values (i.e., clockwise vortex). Increment of the contours is 1. The lines and increment used here are the same as ones shown in the following figures for all of the vorticity plots.

exhibits a large magnitude during the stroke. Note that C_H in two half-strokes is almost equal and in opposite direction, thus making negligible net contribution to the net force. With the increase in D, say $D=1.5$, the magnitudes of C_V and C_H become relatively smaller but still have higher contributions to the forces compared to the other cases in the force reduction and recovery regimes. Thus, the ground effect plays an important role in the force enhancement regime. It is also suggested that insect flight can effectively take advantage of the ground effect to obtain high lift and improve flight efficiency.

On the other hand, based on experimental and numerical results for a normal hovering wing without the ground effect,[20] the profile of C_V exhibits that its peak in the back stroke is higher than one in the forth stroke, similar to the case at $D=5$ in Fig. 6. Thus the back stroke motion contributes major part to C_V during one stroke. However, as shown in Fig. 6 at $D=1$, the profile of C_V over the forth stroke is the same as one over the back stroke. It means that, in the force enhancement regime, both the forth and back stroke motions can contribute large vertical force due to the ground effect.

When $D>1.5$, the force behavior moves to the force reduction regime. As a typical case for $D=2.5$ in Fig. 6, the profile of C_V is relatively small over the stroke, resulting in a low averaged value in Fig. 5. It is seen that C_V in the back stroke becomes somewhat larger than one in the forth stroke. As D increases further, the force behavior, e.g., C_V and C_H at $D=5$ in the force recovery region, is similar to that at $D=\infty$ (Refs. 19 and 20) since the ground effect becomes weak. C_V exhibits a high peak at $t/T=0.8$ approximately in the back stroke compared to that in the forth stroke. It is also noticed that the peak value at $t/T=0.8$ for $D=5$ is higher than one for $D=2.5$. The force reduction at $D=2.5$ is mainly associated with the low distribution in the back stroke and will be further analyzed based on the vortical structures.

B. Ground effect on vortex structures

The vortical structures are closely associated with the aerodynamic characteristics in insect flight.[14–20] In the present problem, there exist the relevant mechanisms of the constraints of the ground for different ground clearances on the leading-edge and trailing-edge vortices (TEV) interacting with previous ones and the flapping foil. The forces on the foil are mainly dependent on the vortical structures near the foil.[38,39] Thus, the vortex structures around the flapping foil are discussed to understand the underlying mechanisms associated with the three force regimes.

To deal with the ground effect on vortex structures, the vorticity contours are shown in Fig. 7 for $D=1$. Since C_V during both the forth and back strokes is the same distribu-

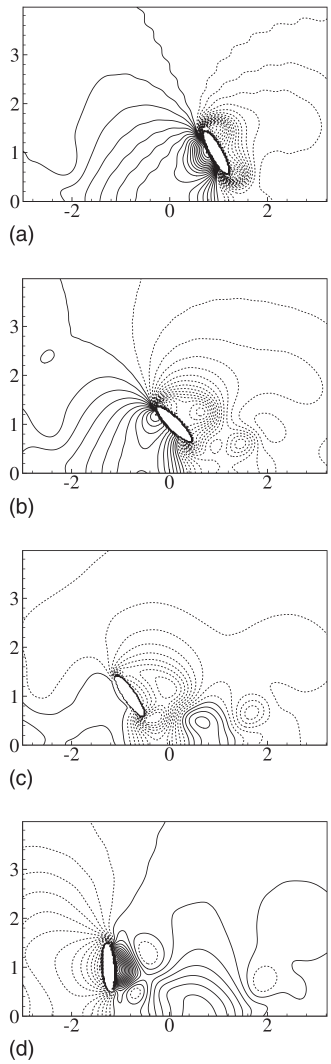

FIG. 8. Relative pressure (i.e., $p-p_{\infty}$) contours during the forth stroke for $D=1$, $\alpha_m=45°$, and $\phi=0°$ at $t/T=$(a) 1/8, (b) 2/8, (c) 3/8, and (d) 4/8. Here, solid lines represent positive values and dashed lines negative values. Increment of the contours is 0.05.

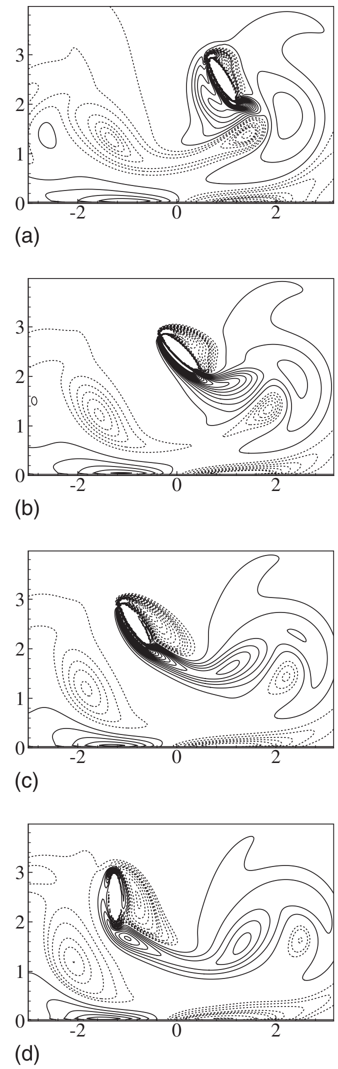

FIG. 9. Vorticity contours during the forth stroke for $D=2.5$, $\alpha_m=45°$, and $\phi=0°$ at $t/T=$(a) 1/8, (b) 2/8, (c) 3/8, and (d) 4/8.

tion at $D=1$ in Fig. 6, we only discuss the time development of vortex structures in the forth stroke. Furthermore, to exhibit the correlation between the vortex structure and force generation, the pressure plots in the field, corresponding to Fig. 7, are also shown in Fig. 8. When the foil takes translation and rotation from $t/T=0$, a negative (or clockwise rotational) LEV is formed gradually and enhanced by the interaction with a positive (or counterclockwise rotational) LEV formed in the previous back stroke. Correspondingly, a lower (or higher) pressure distribution occurs over the downwind (or upwind) side of the foil in Fig. 8(a), resulting in the peaks of C_V and C_H in Fig. 6 at $t/T=1/8$ approximately. The LEV is attached to the foil in accordance with the stall-delayed mechanism and evolved over the downwind side of the foil at $t/T=1/4$ to induce a lower pressure region, associated with a higher C_V. Then, when the foil rotates gradually to a high angle, even $\alpha=90°$ at $t/T=1/2$ in Fig. 7(d), the LEV moves away from the foil and C_V decreases. Correspondingly, as shown in Fig. 8(d), a higher pressure distribution occurs on the right side of the foil, resulting in a large negative C_H at $t/T=1/2$ in Fig. 6. Meanwhile, during the forth stroke, a positive TEV interacts with a negative TEV left in the previous back stroke to form a pair of vortices in Fig. 7(b). Then, the vortex pair is stretched and elongated over the ground, and finally is swept away in the horizontal direction due to their induced velocity. In the back stroke, the time development of vortex structures with an opposite direction is the same as the above description in the forth stroke.

When D increases, Fig. 9 shows the vortex structures for $D=2.5$, lying in the force reduction regime. When the foil moves forward, a negative LEV is formed and attached to the foil during the forth stroke due to the stall-delayed mechanism. Meanwhile, a positive LEV generated in the previous back stroke interacts with the upwind side of the foil at $t/T=1/8$, resulting in the reduction of C_V and C_H in Fig. 6, then combines with the positive TEV at $t/T=2/8$. A vortex pair with the positive TEV and a negative TEV generated in the previous back stroke is formed and moves away along the horizontal-upward direction. The similar evolution of the vortex structures with an opposite direction is also observed in the back stroke.

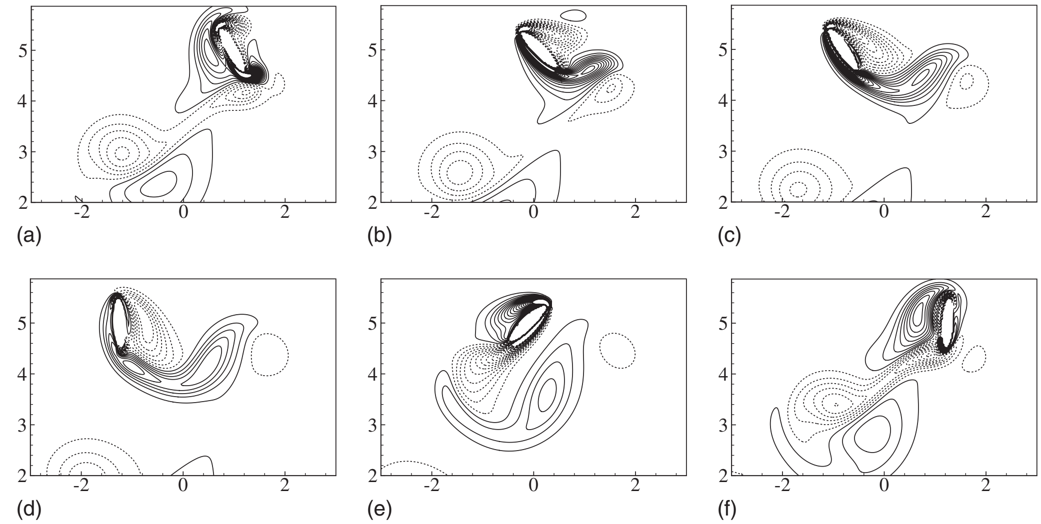

FIG. 10. Vorticity contours during one stroke for $D=5$, $\alpha_m=45°$, and $\phi=0°$ at $t/T=$(a) 1/8, (b) 2/8, (c) 3/8, (d) 4/8, (e) 6/8, and (f) 8/8.

When D increases further, the ground effect becomes weak. As is typically shown in Fig. 10 for $D=5$, the vortex structures near the foil are similar to those at $D=\infty$. When the foil performs translation and rotation in the forth stroke, as exhibited in Figs. 10(a)–10(d), a negative LEV is formed and attached to the foil, and a positive TEV sheds into the wake. When the foil returns in the back stroke, from Figs. 10(e) and 10(f), the negative LEV is evolved over the foil and combined into a shedding TEV, which is coupled with the positive TEV formed in the forth stroke to evolve a stronger vortex pair. Then, the vortex pair moves downward due to their induced velocity. Similar to a reverse von Kármán vortex street in the wake of a flapping foil,[22,23] this vortex-pair structure induces a jetlike mean velocity profile in the wake and is of help in generation of the vertical force. Thus, as shown in Fig. 6, a higher peak of C_V at $t/T=0.8$ approximately occurs in the back stroke.

Basically, from these flow structures shown in Figs. 7, 9, and 10, we can identify that some typical phenomena found experimentally and numerically,[8–20] e.g., dynamic stall delay, foil acceleration in translation and rotation, and interactions between the foil and the existing flow, are closely related to the unsteady forces. The relevant mechanisms have been well discussed in previous work. Here, we mainly reveal different evolved behaviors of the vortex structures due to the ground effect. As shown in Figs. 7(a) and 9(a), when the foil moves forward, the foil interacts with a positive LEV generated in the previous back stroke. At $D=1$, due to the small ground clearance, the LEV in Fig. 7(a) moves over the leading-edge and enhances another negative LEV attached to the foil. As shown in Fig. 6, the strengthened LEV is of help in generation of large C_V. However, at $D=2.5$, the LEV in Fig. 9(a) interacts with the wind side of the foil, resulting in the reduction of C_V. Furthermore, we pay attention to the evolution of vortex pair in Figs. 9 and 10. The vortex pair is coupled by both TEVs with an opposite sign in each half-stroke at $D=2.5$ in Fig. 9 and moves away in the horizontal-upward direction, making against the generation of C_V. Correspondingly, as shown in Fig. 10 for $D=5$, only one vortex pair is observed in one stroke and moves downward to be of benefit to generating a higher C_V.

C. Effect of the phase difference ϕ on force behaviors and vortex structures

The phase difference ϕ between the translation and rotation is an important parameter which is closely related to the vertical force.[20] We further investigate the influence of the phase difference ϕ on the vertical force behaviors and vortex structures with a ground effect. Following the previous description,[20] we refer $\phi=45°$, 0°, and −45° as the advanced, symmetrical, and delayed rotation cases, respectively. The foil motion in these cases differs in the angle of attack at the end of stroke, leading to different force behaviors and vortex structures.

Figure 11(a) shows the time-averaged vertical force coefficient $\bar{C}_V$ versus the phase difference ϕ for three typical values of D. As emphasized in the previous work,[13,20] $\bar{C}_V$ depends sensitively on ϕ. The similar behavior is also revealed with the ground effect. It is seen that $\bar{C}_V$ increases when ϕ varies from −45° to 45° for the same D. Based on our extensive calculations for the advanced and delayed rotation cases, we also identify that there exist three regimes of force behavior, consisting with the classification of the symmetrical rotation case. As shown in Fig. 11(a), the typical values of $\bar{C}_V$ at $D=1$, 2.5, and 5 lie in the force enhancement, force reduction, and force recovery regime, respectively.

The time-dependent vertical force coefficient C_V is shown in Figs. 11(b) and 11(c) for $\phi=45°$ and −45°, respectively. At $D=1$, similar to the profile of C_V in Fig. 6(a) for $\phi=0°$, two peaks of C_V occur, while the phases related to the peaks are different for $\phi=45°$ and −45°. The profile of C_V over the forth stroke is similar to that over the back stroke. With the increase in D, e.g., $D=2.5$ and 5 in Figs. 11(b) and 11(c), there appear two obvious peaks in the stroke. Similar

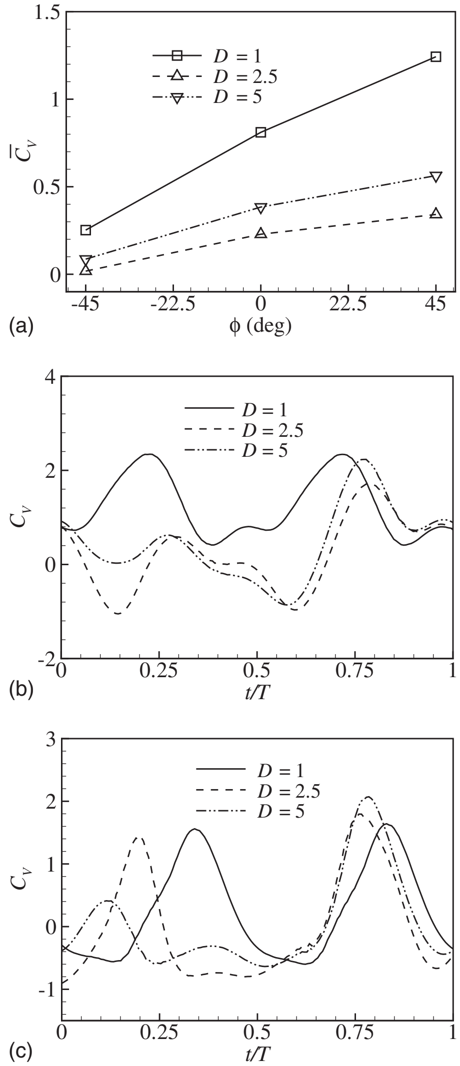

FIG. 11. Vertical force coefficient for different phase differences: (a) mean value $\bar{C}_V$; (b) time-dependent C_V at $\phi=45°$; (c) time-dependent C_V at $\phi=-45°$.

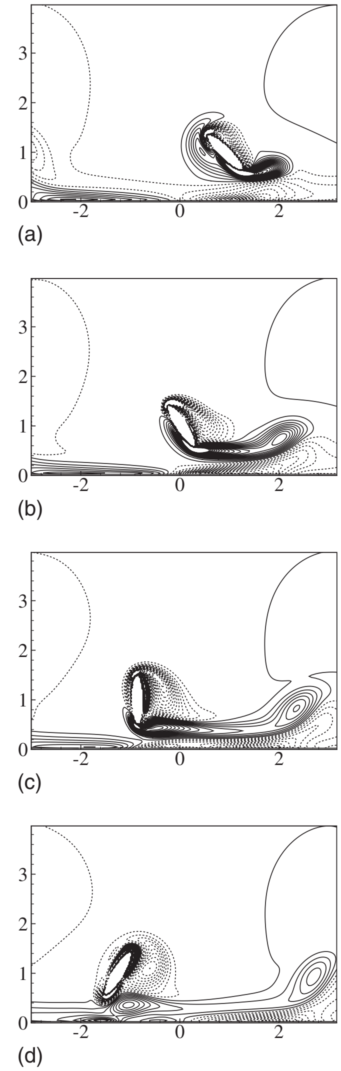

FIG. 12. Vorticity contours during the forth stroke for $D=1$, $\alpha_m=45°$, and $\phi=45°$ at $t/T=$(a) 1/8, (b) 2/8, (c) 3/8, and (d) 4/8.

to Fig. 6(a) in the force reduction and recovery regimes, the highest peak occurs in the back stroke. Thus, the corresponding higher distribution of C_V exists in the back stroke and contributes major part to $\bar{C}_V$. In addition, comparing with the profiles of C_V in the back stroke, the peak value at $D=2.5$ lying in the force reduction regime is less than that at $D=5$ in the force recovery regime.

The vortex structures in the forth stroke are shown in Figs. 12 and 13 at $D=1$ for $\phi=45°$ and $-45°$, respectively. In Fig. 12 for $\phi=45°$, a negative LEV is attached to the foil in accordance with the stall-delayed mechanism, resulting in a higher C_V at $t/T=1/4$ approximately in Fig. 11(b). When the foil is moving to an angle greater than $\pi/2$, e.g., at $t/T=3/8$ and $1/2$ in Fig. 12, the flow separates more quickly and the vertical force C_V becomes lower at $D=1$ and even negative values at $D=2.5$ and 5 in Fig. 11(b). In Fig. 13 for $\phi=-45°$, a positive LEV and a negative TEV formed in the previous back stroke interact with the foil, as shown in Figs. 13(a) and 13(b), respectively. Then, a strong LEV is formed over the foil in Fig. 13(c), resulting in a higher peak of C_V at $t/T=3/8$ approximately in Fig. 11(c). Comparing with the developments of the vortex pair induced by the TEV in Figs. 12, 7, and 13, corresponding to $\phi=45°$, 0°, and $-45°$, respectively, the vortex pair moves the most far away along the ground at $\phi=45°$, which may be also associated with the higher $\bar{C}_V$ in Fig. 11(a).

D. Effect of the rotating amplitude α_m on force behaviors and vortex structures

We further discuss the effect of rotating amplitude α_m on force behaviors and vortex structures with a ground effect. Three amplitudes of rotation $\alpha_m=30°$, 45°, and 60° are considered here. The rotating acceleration for different rotating amplitudes will mainly influence the force acting on the foil and the flow structures near the foil.

The time-averaged vertical force coefficient $\bar{C}_V$ versus the rotating amplitude α_m for three typical values of D is shown in Fig. 14(a). As α_m increases, $\bar{C}_V$ decreases for the same D. In particular, there also exist three regimes of force behavior at $D=1$, 2.5, and 5, corresponding to the force en-

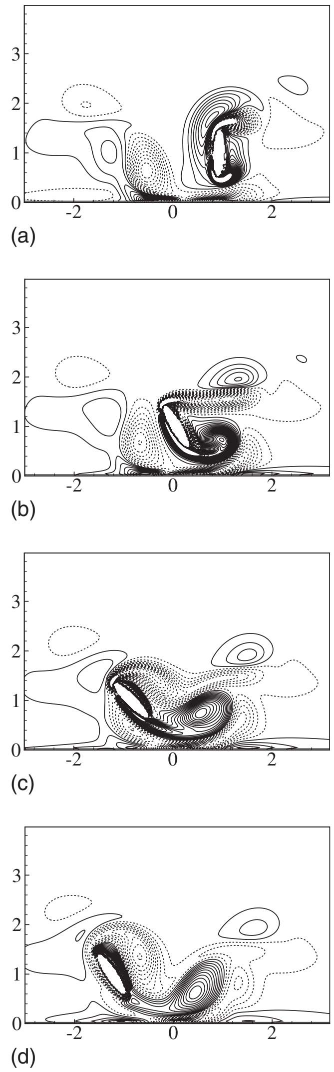

FIG. 13. Vorticity contours during the forth stroke for $D=1$, $\alpha_m=45°$, and $\phi=-45°$ at $t/T=$(a) 1/8, (b) 2/8, (c) 3/8, and (d) 4/8.

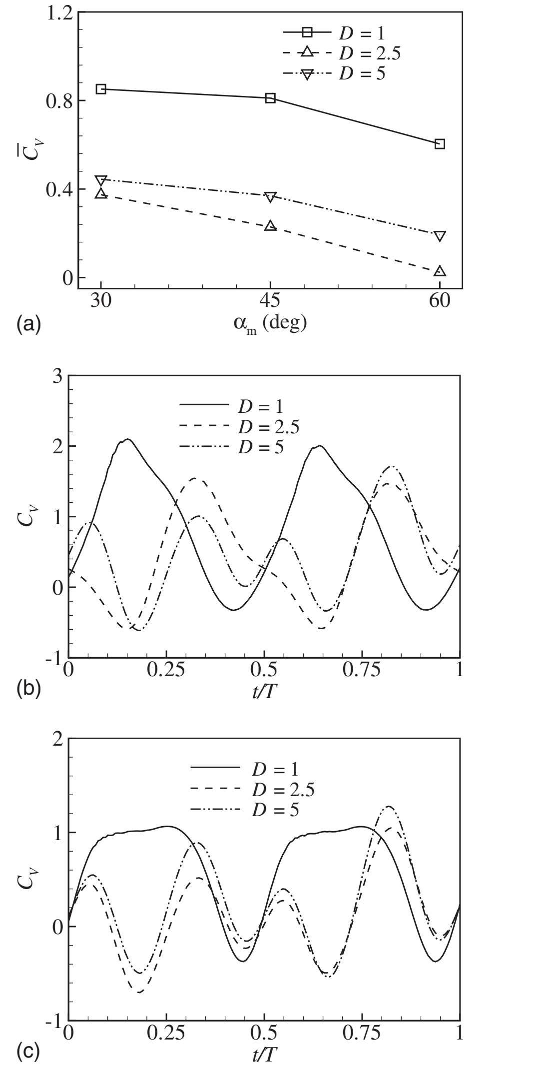

FIG. 14. Vertical force coefficient for different rotating amplitudes: (a) mean value $\bar{C}_V$; (b) time-dependent C_V at $\alpha_m=30°$; (c) time-dependent C_V at $\alpha_m=60°$.

hancement, force reduction, and force recovery regime, respectively. The time-dependent vertical force coefficient C_V is shown in Figs. 14(b) and 14(c) for $\alpha_m=30°$ and 60°, respectively. We can identify two peaks of C_V at $D=1$ and four peaks at $D=2.5$ and 5 over the stroke. From Figs. 14(b) and 14(c) at $D=1$, it is seen that the profile of C_V in the forth stroke is the same as one in the back stroke. Moreover, comparing with the profiles of C_V at $D=1$, unlike the cases for $\alpha_m=30°$ and 45°, a platform distribution of C_V for $\alpha_m=60°$ in Fig. 14(c) occurs over $0.1<t/T<0.3$ approximately in the forth stroke. As D increases, e.g., $D=2.5$ and 5, similar to Fig. 6(a), the highest peaks of C_V in the forth and back strokes occur around $t/T=0.3$ and 0.8, respectively. Comparing with the distribution of C_V over the stroke, relatively major contribution to $\bar{C}_V$ exists in the back stroke.

The evolution of vortex structures for $\alpha_m=30°$ is similar to that for $\alpha_m=45°$ in Fig. 7 and is not shown here. The vortex structures in the forth stroke are shown in Fig. 15 at $D=1$ for $\alpha_m=60°$. Comparing with the vortex structures for $\alpha_m=45°$ in Fig. 7, it is identified that the LEV becomes relatively weak with the increase in α_m, resulting in the decrease in $\bar{C}_V$ in Fig. 14(a). Moreover, as shown in Figs. 15(b) and 15(c), since the angle of attack is relatively small and the TEV moves far away due to the ground effect, the LEV evolves smoothly over the foil and, as mentioned above, induces a platform distribution of C_V during the period $0.1<t/T<0.3$ in Fig. 14(c).

V. CONCLUDING REMARKS

We have investigated insect normal hovering flight in ground effect to provide physical insight into the understanding of aerodynamics and flow structures for insect normal hovering flight and flying mechanisms relevant to insect perching on body. The ground effect on the unsteady forces and vortical structures is analyzed. Here, we briefly summarize the results obtained in the present study and discuss the underlying mechanisms in the normal hovering with the ground effect.

According to the mean force behavior, we have identified three typical regimes, including force enhancement, force reduction, and force recovery regime. As typically

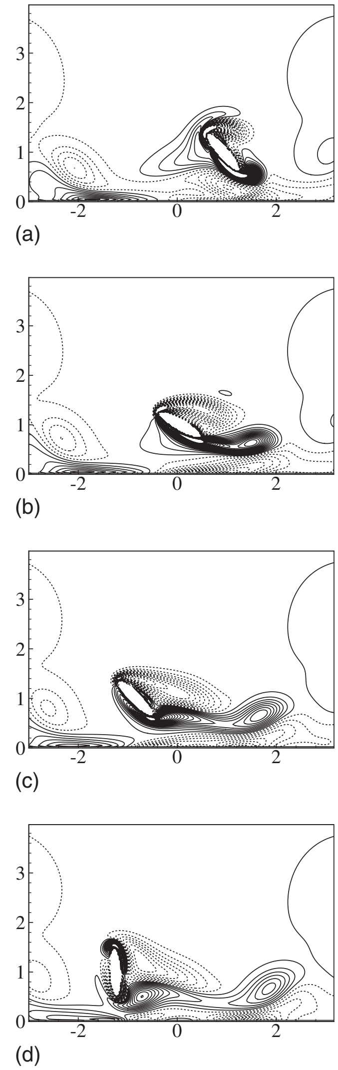

FIG. 15. Vorticity contours during the forth stroke for $D=1$, $\alpha_m=60°$, and $\phi=0°$ at $t/T=$(a) 1/8, (b) 2/8, (c) 3/8, and (d) 4/8.

shown in Fig. 5, when the ground clearance increases, the mean vertical force $\bar{C}_V$ decreases quickly to a minimum, then increases gradually and approaches to the value without the ground effect. This behavior differs from the flow past a pitching foil near a ground,[31,32] where the normal force acting on the foil decreases monotonously with the increase in the ground clearance. Moreover, by means of extensive calculations for different phase differences, i.e., the advanced, symmetrical, and delayed rotation cases, and for different amplitudes of rotation, we have identified that there still exist the three force regimes.

The force characteristics are closely associated with vortical structures. Some typical phenomena, e.g., dynamic stall delay, foil acceleration in translation and rotation, and interactions between the foil and the existing flow, are observed and closely related to the forces. In the force enhancement regime, the interaction between the existed vortex and the foil can enhance the LEV and is of benefit to generating a high vertical force. In the force reduction regime, the vortex pair coupled by the existed vortex and the TEV moves away in the horizontal-upward direction due to the ground effect, resulting in the reduction of the vertical force. Moreover, in the force recovery regime, the vortex pair induces a jetlike mean velocity profile in the wake, similar to the vortex structure without the ground effect[20] and is of help in the generation of higher vertical force in the back stroke.

Based on the results obtained for different ground clearances, phase differences, and amplitudes of rotation, we can understand the flying mechanisms relevant to insect perching on body. Basically, the present results are qualitatively consistent with our observation of fruit fly perching on body by means of high-speed charge-coupled devices. When insect takes off the body, the insect may prefer to have a flight with the advanced rotation and relatively small amplitude of rotation, which are associated with high vertical force, e.g., as shown in Figs. 11(a) and 14(a). In contrast, when insect lands on the body, the insect may select preferably a flight with the symmetrical or delayed rotation and relatively large amplitude of rotation, which are related to small vertical force.

The results obtained in this study are helpful to understand aerodynamics and flow structures for insect normal hovering flight with a ground effect and flying mechanisms relevant to insect perching on body. However, the flow characteristics in this problem are certainly far more complex and diverse than the simple model considered here. Ideally, 3D computation of a flapping wing in ground effect is desirable and is a target in our further work.

ACKNOWLEDGMENTS

This work was supported by the Innovation Project of the Chinese Academy of Sciences (Contract No. KJCX2-YW-L05), the National Natural Science Foundation of China (Contract Nos. 90605005 and 90405007), and Program for Changjiang Scholars and Innovative Research Team in University. The authors thank the referees for their valuable comments.

[1] A. K. Brodsky, *The Evolution of Insect Flight* (Oxford University Press, Oxford, 1994).
[2] Y. S. Lian, W. Shyy, D. Viieru, and B. N. Zhang, "Membrane wing aerodynamics for micro air vehicles," Prog. Aerosp. Sci. **39**, 425 (2003).
[3] N. Kato and S. Kamimura, *Bio-mechanisms of Swimming and Flying* (Springer, Tokyo, 2007).
[4] T. Weish-Fogh and M. Jensen, "Biology and physics of locust flight. Basic principles of insect flight: a critical review," Philos. Trans. R. Soc. London **239**, 415 (1956).
[5] R. B. Srygley and A. L. R. Thomas, "Unconventional lift-generating mechanisms in free-flying butterflies," Nature (London) **420**, 660 (2002).
[6] R. J. Bomphrey, N. J. Lawson, G. K. Taylor, and A. L. R. Thomas, "Application of digital particle image velocimetry to insect aerodynamics: measurement of the leading-edge vortex and near wake of a hawkmoth," Exp. Fluids **40**, 546 (2006).
[7] M. H. Dickinson and K. G. Götz, "Unsteady aerodynamic performance of model wings at low Reynolds numbers," J. Exp. Biol. **174**, 45 (1993).
[8] M. H. Dickinson, "The effects of wing rotation on unsteady aerodynamic performance at low Reynolds number," J. Exp. Biol. **192**, 179 (1994).
[9] C. P. Ellington, C. van den Berg, A. P. Willmott, and A. L. R. Thomos, "Leading-edge vortices in insect flight," Nature (London) **384**, 626 (1996).
[10] S. P. Sane and M. H. Dickinson, "The control of flight force by a flapping wing: lift and drag production," J. Exp. Biol. **204**, 2607 (2001).
[11] J. M. Birch and M. H. Dickinson, "Spanwise flow and the attachment of the leading-edge vortex on insect wings," Nature (London) **412**, 729 (2001).
[12] S. P. Sane and M. H. Dickinson, "The aerodynamic effects of wing rota-

tion and a revised quasi-steady model of flapping flight," J. Exp. Biol. **205**, 1087 (2002).
[13]M. H. Dickinson, F. O. Lehmann, and S. P. Sane, "Wing rotation and the aerodynamic basis of insect flight," Science **284**, 1954 (1999).
[14]H. Liu and K. Kawachi, "A numerical study of insect flight," J. Comput. Phys. **146**, 124 (1998).
[15]H. Liu, C. P. Ellington, K. Kawachi, C. van den Berg, and A. P. Willmott, "A computational fluid dynamics study of hawkmoth hovering," J. Exp. Biol. **201**, 461 (1998).
[16]Z. J. Wang, "Two-dimensional mechanism of hovering," Phys. Rev. Lett. **85**, 2216 (2000).
[17]M. Sun and J. Tang, "Unsteady aerodynamic force generation by a model fruit fly wing in flapping motion," J. Exp. Biol. **205**, 55 (2002).
[18]R. Ramamurit and W. C. Sandberg, "A three-dimensional computation study of the aerodynamic mechanisms of insect flight," J. Exp. Biol. **205**, 1507 (2002).
[19]Z. J. Wang, "The role of drag in insect hovering," J. Exp. Biol. **207**, 4147 (2004).
[20]Z. J. Wang, J. M. Birch, and M. H. Dickinson, "Unsteady forces and flows in low Reynolds number hovering flight: two-dimensional computations vs robotic wing experiments," J. Exp. Biol. **207**, 449 (2004).
[21]S. Xu and Z. J. Wang, "An immersed interface method for simulating the interaction of a fluid with moving boundaries," J. Comput. Phys. **216**, 454 (2006).
[22]X. Y. Lu and Q. Liao, "Dynamic responses of a two-dimensional flapping foil motion," Phys. Fluids **18**, 098104 (2006).
[23]G. J. Dong and X. Y. Lu, "Characteristics of flow over traveling-wavy foils in a side-by-side arrangement," Phys. Fluids **19**, 057107 (2007).
[24]F. M. Bos, D. Lentink, B. W. van Oudheusden, and H. Bijl, "Influence of wing kinematics on aerodynamic performance in hovering insect flight," J. Fluid Mech. **594**, 341 (2008).
[25]M. Sun and S. L. Lan, "A computational study of the aerodynamic forces and power requirements of dragonfly (*Aeschna juncea*) hovering," J. Exp. Biol. **207**, 1887 (2004).
[26]T. Gao, Y.-H. Tseng, and X. Y. Lu, "An improved hybrid Cartesian/immersed boundary method for fluid-solid flows," Int. J. Numer. Methods Fluids **55**, 1189 (2007).
[27]Y. Sui, Y. T. Chew, P. Roy, and H. T. Low, "A hybrid immersed-boundary and multi-block lattice Boltzmann method for simulating fluid and moving-boundaries interactions," Int. J. Numer. Methods Fluids **53**, 1727 (2006).
[28]Y. Sui, Y. T. Chew, P. Roy, X. B. Chen, and H. T. Low, "Transient deformation of elastic capsules in shear flow: Effect of membrane bending stiffness," Phys. Rev. E **75**, 066301 (2007).
[29]Z. G. Feng and E. E. Michaelides, "The immersed boundary-lattice Boltzmann method for solving fluid-particles interaction problems," J. Comput. Phys. **195**, 602 (2004).
[30]Z. G. Feng and E. E. Michaelides, "Proteus: a direct forcing method in the simulations of particulate flows," J. Comput. Phys. **202**, 20 (2005).
[31]J. Zerihan and X. Zhang, "Aerodynamics of gurney flaps on a wing in ground effect," AIAA J. **39**, 772 (2001).
[32]Y. Moryossef and Y. Levy, "Effect of oscillations on airfoils in close proximity to the ground," AIAA J. **42**, 1755 (2004).
[33]C. S. Peskin, "Flow patterns around heart valves: a numerical method," J. Comput. Phys. **10**, 252 (1972).
[34]C. S. Peskin, "The immersed boundary method," Acta Numerica **11**, 479 (2002).
[35]S. Chen and G. D. Doolen, "Lattice Boltzmann method for fluid flows," Annu. Rev. Fluid Mech. **30**, 329 (1998).
[36]Z. L. Guo, C. G. Zheng, and B. C. Shi, "Discrete lattice effects on the forcing term in the lattice Boltzmann method," Phys. Rev. E **65**, 046308 (2002).
[37]Y. Qian, D. d'Humieres, and P. Lallemand, "Lattice BGK models for Navier–Stokes equation," Europhys. Lett. **17**, 479 (1992).
[38]J. Z. Wu, Z. L. Pan, and X. Y. Lu, "Unsteady fluid-dynamic force solely in terms of control surface integral," Phys. Fluids **17**, 098102 (2005).
[39]J. Z. Wu, X. Y. Lu, and L. X. Zhuang, "Integral force acting on a body due to local flow structures," J. Fluid Mech. **576**, 265 (2007).